Investigation of He retention in W through combined He characterization methods and cluster dynamics model*

Jie Qiu,[1,2] Xun-Xiang Hu,[3,4] Cong-Yi Li,[5,2,†] Wendy Garcia,[2] Tan Shi,[6] Sha Xue,[7] Jamie L. Weaver,[8] H. Heather Chen-Mayer,[8] and Brian D. Wirth[2,4]

[1]*SJTU Paris Elite Institute of Technology, Shanghai Jiao Tong University, Shanghai, 200240, China*
[2]*Department of Nuclear Engineering, University of Tennessee, Knoxville, TN 37996 USA*
[3]*School of Physics, Sichuan University, Chengdu, Sichuan, China 610065*
[4]*Oak Ridge National Laboratory, Oak Ridge, TN 37830 USA*
[5]*Global Institute of Future Technology, Shanghai Jiao Tong University, Shanghai, 200240, China*
[6]*School of Nuclear Science and Technology, Xi'an Jiaotong University, Xi'an, 710049, China*
[7]*Nuclear Engineering Program, The Ohio State University, Columbus, OH 43210 USA*
[8]*Material Measurement Laboratory, National Institute of Standards and Technology, Gaithersburg, MD 20899 USA*

Tungsten (W) is the leading plasma-facing candidate material for the International Thermonuclear Experimental Reactor (ITER) and next-generation fusion reactors. The impact of synergistic helium (He), irradiation-induced microstructural changes, and the corresponding thermal-mechanical property degradation of W are critically important but are not well understood yet. Predicting the performance of W in fusion environments requires understanding the fundamentals of He–defect interactions and the resultant He bubble nucleation and growth in W. In this study, He retention in helium-ion-implanted W was assessed using neutron depth profiling (NDP), laser ablation mass spectrometry (LAMS), and thermal desorption spectroscopy (TDS) following 10 keV room-temperature He implantation at various fluences. These three experimental techniques enabled the determination of the He depth profile and retention in He-implanted W. A cluster dynamics model based on the diffusion-reaction rate theory was applied to interpret the experimental data. The model successfully predicted the He spatial depth-dependent profile in He-implanted W, which was in good agreement with the LAMS measurements. The model also successfully captured the major features of the He desorption spectra observed in the THDS measurements. The NDP quantified total He concentration values for the samples; they were similar to those estimated by LAMS. However, the depth profiles from NDP and LAMS were not comparable due to several factors. The combination of modeling and experimentation enabled the identification of possible trapping sites for He in W and the evolution of He-defect clusters during the TDS thermal annealing process.

Keywords: Tokamak, Nuclear reactor, Nondestructive detection

I. INTRODUCTION

Tungsten is a leading candidate plasma-facing material for nuclear fusion environments because of its high melting point, low sputtering yield, high thermal conductivity, and low tritium (^{3}H) retention rate under non-irradiated conditions [1]. Exposure to the 14.1 MeV-peaked neutron spectrum in an operational fusion reactor produces significant microstructural changes in W, which arise from the production and diffusional evolution of various intrinsic radiation defects and transmutant He and H because of (n, α) and (n, p) nuclear reactions, as well as solid transmutant elements (for example, Rhenium and Osmium) [2]. More importantly, the W plasma-facing components are bombarded by low-energy and high-flux He and H particles that diffuse from the fusion plasma [3]. The synergistic interactions among radiation damage, evolving composition, and gaseous species significantly impact the performance of W plasma-facing components [1, 4–7]. Although He behavior in W has been extensively studied, a comprehensive understanding is lacking. Topics requiring further investigation include the energetics and kinetics of He–defect interactions, He retention and depth profiling, and He-bubble nucleation and growth.

Theoretical atomistic simulations have been widely used to investigate the energetics and kinetics of He–defect interactions in W [8, 9]. Kinetic Monte Carlo [10] and cluster dynamics [11, 12] modeling have been used to model the evolution of He-defect clusters resulting from the migration of mobile species across longer time scales, in addition to atomistic molecular dynamics simulations [8, 13, 14]. Thermal desorption spectroscopy (TDS) has been the main experimental characterization technique for investigating He behavior in W. TDS can reveal interactions between irradiation defects and He by identifying possible trapping sites for He in materials when combined with energetic data from atomistic simulations [15]. This experimental technique can provide information such as He retention in a specific temperature regime and a rough estimation of the activation energies corresponding to the desorption peaks using a first-order kinetics model. The close coordination of the TDS and cluster dynamics modeling can reveal the underlying mechanisms controlling the He desorption spectra [11, 16]. However, the spatial information of the He distribution in W is not available from the TDS. Other experimental techniques, such as neu-

---

tron depth profiling (NDP) and laser ablation mass spectrometry (LAMS) [17], are required to obtain the He spatial distribution and the experimental data for validating the model.

In this study, we combined three He characterization techniques (NDP, LAMS, TDS) with a cluster dynamics model to systematically investigate He retention, migration, and defect cluster evolution in He ion-implanted W. The He concentration depth profiles and thermal desorption spectra of He-implanted W were measured. A cluster dynamics model based on the diffusion-reaction rate theory was compared to the experimental results, and the agreement between them detailed the Hedefect evolution and He diffusion during He implantation and the subsequent thermal annealing process. This work aims to 1) demonstrate the requirement of various experimental techniques to fully characterize He in W; 2) validate the energetic and kinetic parameters describing the interactions between He and defects; and 3) explore the underlying mechanisms controlling He-defect cluster evolution in W, which are critically important for predicting the nucleation and growth of He bubbles in W when employed in fusion environments.

II. RESEARCH APPROACH: EXPERIMENTAL AND COMPUTATIONAL METHODS

A. Materials

The samples used in this study had ultrahigh purity ($\approx$ 99.99 wt. % W, wt. % = mass of W in grams relative to the mass of total sample material in grams) polycrystalline W disks with $4.5\,\mathrm{mm}$ diameter and $1\,\mathrm{mm}$ thickness (Goodfellow) and a grain size of $\approx 1.25\,\mathrm{\mu m}$. Samples were annealed at $1000\,^\circ\mathrm{C}$ in a vacuum environment ($\approx 1.3 \times 10^{-4}\,\mathrm{Pa}$, $1\,\mathrm{Pa}$ $\approx 7.5 \times 10^{-3}\,\mathrm{torr}$) for $1\,\mathrm{h}$ after polishing to a mirror surface with a final finishing of $\approx 0.5\,\mathrm{\mu m}$. The estimated grain size post-annealing was $\approx 1.75\,\mathrm{\mu m}$. $10\,\mathrm{keV}$ He-3 (^{3}He, for NDP) and He-4 (^{4}He) ion implantation were performed at room temperature under vacuum conditions of $\approx 10^{-7}\,\mathrm{torr}$ using a $20\,\mathrm{keV}$ noble-gas feeding ion gun with a beam-raster scanning area of $0.2\,\mathrm{cm}^2$. The ion gun was installed on an ORNL-UTK Joint Gas Implantation and Thermal Desorption System (GITDS) [18]. Three different fluence levels (5×10^{14} He atoms cm^{-2}, 3×10^{15} He atoms cm^{-2}, 1×10^{16} He atoms cm^{-2}) were considered with a fluence rate (aka flux) of $\approx 3\times10^{12}$ He atoms $\mathrm{cm}^{-2}\mathrm{s}^{-1}$ for both ^{3}He and ^{4}He ion implantations. Note that the units that include He atoms herein are shortened to He. Figure 1 shows the Stopping and Range of Ions in Matter (SRIM) calculation (ion distribution and quick calculation of damage) of the He depth profiles and the vacancy production rate in $10\,\mathrm{keV}$ ^{3}He-and ^{4}He-implanted W, respectively. Figure 1 reveals similar profiles for both ^{3}He and ^{4}He; however, ^{4}He exhibits more vacancies than ^{3}He under the same implantation energy.
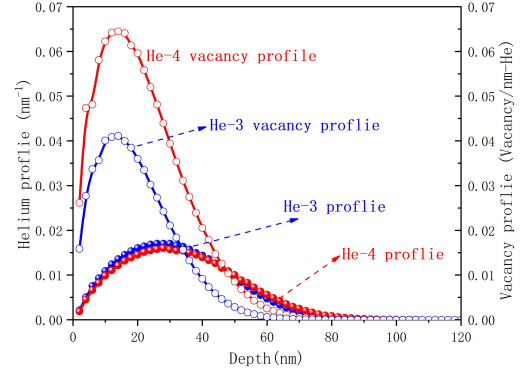

Fig. 1. (Color online) SRIM calculation of the implanted He profile and vacancy production rate of $10\,\mathrm{keV}$ ^{3}He and ^{4}He in W.

B. Thermal desorption spectroscopy

Thermal He desorption measurements were performed on ^{4}He ion-implanted W using the ORNL-UTK Joint GITDS [18]. The baseline pressure of the TDS system was $\approx 1 \times 10^{-9}\,\mathrm{torr}$. The temperature profile used for the ^{4}He-implanted samples was consistent with that for the NDP samples (^{3}He -implanted ones), i.e., increasing sample temperature to $1000\,^\circ\mathrm{C}$ with a heating rate of $^\circ\mathrm{Cs}^{-1}$ and then holding at $1000\,^\circ\mathrm{C}$ for $1\,\mathrm{h}$. The desorbed He was captured using a quadrupole mass spectrometer and calibrated by employing a VTI standard He leak. The recorded He desorption spectra provided data to validate the developed model. He retention and the thermal stability of He-defect complexes in W from room temperature to $1000\,^\circ\mathrm{C}$ could be assessed from the He desorption spectra.

C. Neutron depth profiling

A $1\,\mathrm{h}$ vacuum annealing at $1000\,^\circ\mathrm{C}$ was performed following the room-temperature implantation of $10\,\mathrm{keV}$ ^{3}He on the samples sent to the National Institute of Standards and Technology (NIST) Material Measurement Laboratory and NIST Center for Neutron Research (NCNR) for NDP measurements. NDP [19] is a nominally nondestructive isotopic characterization technique that can be used to estimate the spatial distribution of He in W following a heat treatment [20]. This technique relies on the large thermal neutron absorption cross-section ($5333\,\mathrm{barns}$, $1\,\mathrm{barn} = 1 \times 10^{-28}\,\mathrm{m}^2$ [19]) of ^{3}He. This enables the mapping of the distribution and concentration of He atoms in W by measuring the final kinetic energy of the proton (p), produced from the nuclear reaction between neutrons and ^{3}He, after it has passed through the material. A schematic of the interior of the NDP instrument is shown in Figure 2 (adapted from Ref. [21]).

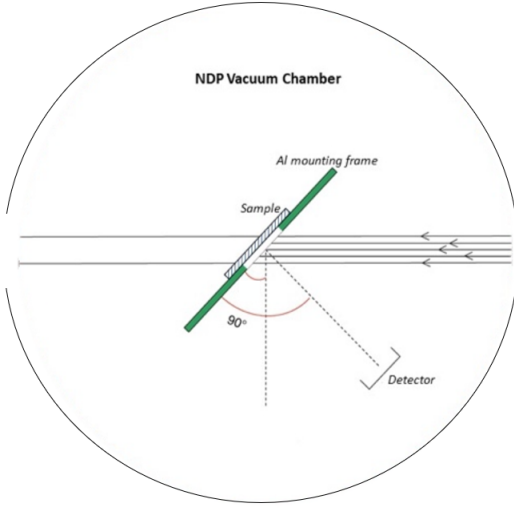NDP was conducted at the cold NDP (cNDP) station at the end of Neutron Guide-5 at NCNR. The sample was attached

Fig. 2. (Color online) Planar view of the NDP facility at NIST, as reproduced from Ref. [21].

to a supported Teflon aperture ($\approx 3\,$mm in diameter, and the results are the average values across this diameter) in the center of the vacuum chamber facing a Si-barrier detector (OR-TEC). This detector, with an active area of $150\,$mm^2, ia $\approx 10\,$cm away from the neutron beam spot on the sample and has an energy resolution of $\approx 18\,$keV. The ^{3}He atoms in W absorb a cold neutron and emit ^{3}He and p particles with initial kinetic energies according to the following nuclear reaction:

$$^3\text{He} + neutron \rightarrow proton(p, 572\,\text{keV}) + triton(^3\text{He}, 191\,\text{keV}). \tag{1}$$
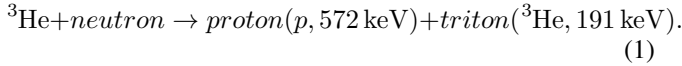
The electronic stopping force for the p, the ion profile analyzed in this study, and 3 H in W were $160\,$keV μm^{-1} at $572\,$keV and $290\,$keV μm^{-1} at $191\,$keV, respectively, as calculated by SRIM [22, 23]. These charged particles predominantly lost energy through inelastic Coulombic interactions with atomic electrons along the outward path from the reaction sites. The detector recorded the count rate and residual energy of the detected charged particles simultaneously (Figure 2). The charged particles lost negligible energy after leaving the surface of the sample because the chamber was maintained at a vacuum level of $< 10^{-6}\,$torr. Energy loss was an indicator of the path length traveled by the particles within the sample. The Transport Range of Ions in Materials (TRIM) code was used to estimate the path length. Theoretically, both p and ^{3}H spectra can be used to determine the ^{3}He profile in W. The profile from the ^{3}H spectrum provides more detailed information than the p spectrum because the stopping power of ^{3}H is much larger than that of p. However, the ^{3}H energy ($191\,$keV) was low and difficult to distinguish from low-energy noise in the spectra. Therefore, the p spectrum was used to analyze the ^{3}He spatial distribution.

The concentration of ^{3}He in the sample was obtained by comparing the count rate measured from the sample with that of a well-characterized in-house ^{10}B concentration standard sample [19]. All NDP data were normalized to data from

a neutron fluence rate monitor with corrected deadtime and background and, when necessary, normalized to their aperture size. The measured profiles were average values relative to the size of the aperture. Long-neutron-beam exposure times (several tens of hours) were used to minimize uncertainty in the statistical counting of the charged particles ($\approx 1\,\%$, 1σ). For the nuclear reaction shown in Eq(1), the Q value is approximately $764\,$keV, whereas the energy of the incident neutron is below $5\,$meV. Thus, the incident neutron energy is too small to perturb ^{3}He from its original reaction site or significantly move the center of mass in the reaction.

D. Laser Ablation Mass Spectrometry (LAMS)

LAMS was used to quantify the retention and depth profiles of the gaseous species in the W samples [17]. ^{4}He ion-implanted W samples were first cleaned with acetone, followed by isopropyl alcohol, and then adhered by Kapton tape to a flat stainless-steel sample holder. The LAMS chamber was pumped to a vacuum of the order of $10^{-8}\,$torr before testing. A $60\,$mJ, $532\,$nm, Nd:YAG laser was used at 3% power, $1.8\,$mJ s^{-1} ($1\,$mJ s^{-1} = 1 W), to produce a $1\,$Hz, $5\,$ns pulse. A plasma plume composed of elements ablated by the laser pulse was produced as it impinged on the W sample surface. The vacuum system guided the ablated gaseous species from the LAMS sample chamber to a quadruple mass spectrometer, where the species were identified and quantified. These experiments were uncertain due to the crater shape and volume created by the laser ablation process. The volume was calculated by microscopic observation but had similar uncertainty, as discussed in detail below.

The reliability of He depth profiling using LAMS is critically dependent on the correlation between the crater volume and the number of accumulated ablations that generate the crater. For this study, crater volume calibration was performed on a W control sample prepared with the same surface finish as the He-implanted samples. The ablated crater volumes were calculated as a function of the number of laser ablation pulses by measuring the crater depth, bottom inner width, upper outer width, and average width at the surface using a Keyence optical microscope. The He signal captured by the mass spectrometer following each ablation was converted to atomic flux using the same calibration procedure as for TDS. The integration of the He atomic flux over the He peak duration gave the total amount of He in a single ablation, which was then divided by the corresponding ablation volume to calculate the concentration. Further information on the calibration can be found in [17, 24]. Six consecutive ablations per location were performed on the He-implanted samples, resulting in a final characterization depth of approximately $900\,$nm and a crater width of $\approx 50\,\mu$m. The depth-dependent He concentration was measured by averaging nine different spatial locations in the sample to ensure sufficient statistical data.

E.   Cluster dynamics modeling

A cluster dynamics model based on the diffusion-reaction rate theory was used in this study to predict the He-defect cluster evolution in W in coordination with the experimental characterization results. This model, developed by Xu and Wirth [25–27], is based on the classical rate theory for computing one-dimensional (1D) time- and space-dependent volumetric concentrations (in nm^{-3}) of defect clusters under various irradiation or post-irradiation annealing conditions. It can incorporate vacancies, self-interstitials, and He clusters with sizes up to tens of thousands and has flexibility in terms of the number of mobile species and transformations. reaction kinetics and constants are assumed to be isotropic in nature and are most suitable for the three-dimensional motion of defect clusters. This model and its corresponding modified versions have been applied to simulate He defect interactions in He-implanted iron [25, 26], defect evolution in $1\,MeV$ Kr+ irradiation in thin Mo foils [28] and neutron-irradiated high-purity iron [29]. Details of this model are available in [26, 29]. Here, we expand the application of this model to study He–vacancy interactions in He-implanted W.

In this study, clusters of interstitials (I), vacancies (V), He, and He-V complexes, as well as the reactions that result in their transformation, are considered. Three numbers, NI, NV, and NHe, were selected to define the maximum phase space. Only reactions and clusters contained in this predefined phase space were considered. Mobile species considered in this model include single W self-interstitials atom (SIA) (I_1), di- and tri-SIA (I_2, I_3), single vacancy (V_1), interstitial He atom (He_1) and small clusters of interstitial He atoms (He_2, He_3, He_4, He_5). Other defects, including He-V clusters, V clusters, and large helium clusters (He_x, where x > 5), were considered immobile. Table 1 lists the pre-factors of the diffusivities and migration energies (eV) of the mobile species used in the current model. These values are consistent with the atomistic modeling of W [11].

The source term for the radiation-induced defects is highly dependent on the implantation energy. At high implantation energies (several MeV), the effect of the collision cascade must be properly treated. However, at low implantation energies (several to a few tens of keV), spatially dependent Frenkel pair production is assumed, and the SRIM calculation results are used as the input for both radiation-induced defects and implanted He in the cluster dynamics model [28]. The reactions among the clusters included in the model involved cluster generation via small clusters capturing mobile species or the dissociation of larger clusters, annihilation by capturing mobile species leading to recombination, or dissociation by emitting a single I, V, or He. This high-pressure cluster ejects a surrounding W lattice atom to form a He-vacancy cluster if a cluster of interstitial He atoms grows by capturing other mobile interstitial He atoms and reaches a critical size. This process is known as trap mutation [30]. The maximum size of the interstitial He cluster has been fixed at He_9 in this study, although molecular dynamics (MD) simulations have indicated that in proximity to free surfaces, trap mutations can occur at much smaller sizes [30]. Any He cluster containing more than nine He atoms spontaneously transforms into He_xV. The construction of partial differential equations describing the evolution of the defined clusters is based on classical rate theory. The binding energies for small He–V clusters are based on the values from several computational and theoretical models [9, 31]. For large clusters, the binding energies are extrapolated from the existing binding energy values for smaller clusters [11]. To identify the key parameters that affect the accuracy of model predictions, parameter optimization was performed within a reasonable range for the following parameters: the migration energy of a single vacancy and the binding energies of small He-V clusters.

III.   EXPERIMENTAL RESULTS

A.   Thermal He desorption spectra of [4]He implanted W

The measured He desorption spectra from the $10\,keV$ [4]He-implanted W with three different fluences during the $1000\,°C$ 1 h heat treatment process are shown in Figure 3. Background noise from the mass spectrometer was the main source of scatter in the raw data. [4]He implantation occurred due to a low signal-to-noise level in the TDS and the very low amount of desorbed He from room temperature (RT, $\approx 23\,°C$) to $1000\,°C$. The differences in the desorption spectra of the [3]He- and [4]He-implanted W are discussed in Section IV C based on cluster dynamics modeling predictions.
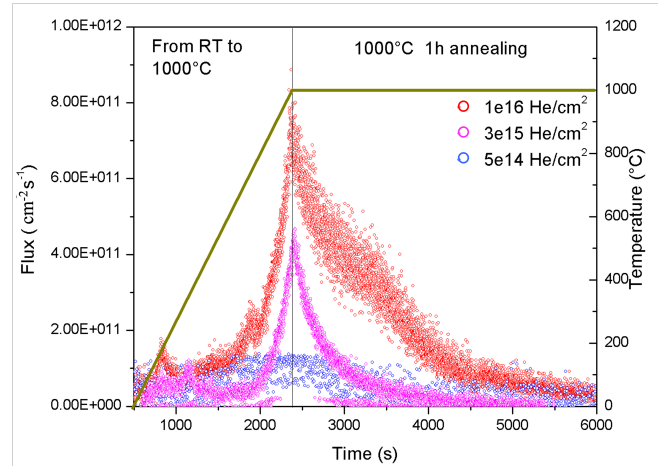

Fig. 3. (Color online) [4]He desorption peak during $1000\,°C$ 1 h annealing process measured by TDS; the solid green line shows the temperature profile and the red, magenta, and blue circles show the He desorption flux as a function of implanted He fluence. Uncertainty is based on the equipment calibration and is less than 5% (not shown).

A general observation from Figure 3 is that the He desorption flux increases with the He implantation fluence. The He desorption signals of W implanted at 1×10^{16} He cm^{-2} and 3×10^{15} He cm^{-2} are apparent, whereas the He desorption signal of the lowest fluence sample has a low level just above the background. For the sample implanted to

Mobile species	I_1	I_2	I_3	V_1	He_1	He_2	He_3	He_4	He_5
Migration energy(eV)	0.009	0.024	0.033	1.29	0.13	0.20	0.25	0.20	0.12
Pre-factor($cm^2 s^{-1}$)	3.92	7.97	8.77	177	2.95	3.24	2.26	1.68	5.20

Table 1. Mobile species and their migration energies and pre-factors used in the cluster dynamic model.
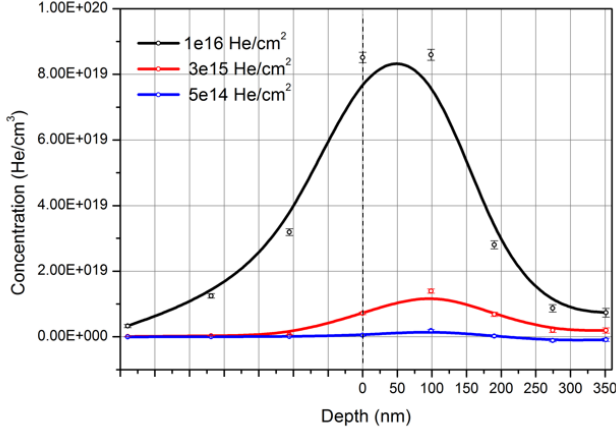

Fig. 4. (Color online) NDP depth profile of ^{3}He in W implanted at $10\,keV$ ^{3}He to fluences of 5×10^{14} ^{3}He cm^{-2}, 3×10^{15} ^{3}He cm^{-2} and 1×10^{16} ^{3}He cm^{-2}, respectively, following $1\,h$ $1000\,^\circ C$ annealing. The data has been binned to the resolution of the NDP detector ($\approx 18\,keV$). Uncertainty bars are 1σ and are based on experimental counting statistics. The dashed black line indicates the surface of the sample and the beginning of the ^{3}He profile. Solid lines were added for reference and do not represent a mathematical fit.

1×10^{16} He cm^{-2}, a small He desorption peak is evident at $200\,^\circ C$ and a shoulder develops at $\approx 620\,^\circ C$ followed by a continuous increase of the He flux up to the maximum temperature of $1000\,^\circ C$, resulting in an incompletely developed He desorption peak in the linear temperature ramping process from $700\,^\circ C$ to $1000\,^\circ C$. The measured He flux starts decreasing and finally reaches and remains at the background level when the maximum temperature is attained. Similar features were observed in the He desorption spectra of the other two samples. For 3×10^{15} He cm^{-2} sample, a small peak around $200\,^\circ C$ was also captured along with a 2nd small peak at $\approx 320\,^\circ C$. No He desorption shoulders were observed in the spectrum. Similarly, the He desorption flux increased in the linear temperature-ramping regime up to the maximum temperature and decreased to the background level during the high-temperature annealing process. For the lowest fluence sample, the detailed features of the spectra could not be deconvolved from the measured signals because the desorbed He was close to the system resolution.

B. ^{3}He depth profiling determined by NDP

Figure 4 represents the He depth profiles in W samples implanted with ^{3}He at three different fluences following $1\,h$ $1000\,^\circ C$ annealing, as measured by NDP. Note that the nonzero experimental data above the sample surface (depth < 0) are caused by signal broadening and do not represent the actual He content. Measurable ^{3}He depth profiles were obtained for the samples implanted at fluences of 3×10^{15} ^{3}He cm^{-2} and 1×10^{16} ^{3}He cm^{-2}. In these samples, the ^{3}He concentration peaked at a depth of approximately $30\,nm$ to $50\,nm$ and extended to more than $200\,nm$. The profile of the ^{3}He implant sample at the lowest fluence could not be well-resolved from the background signal. NDP results for the as-implanted W samples were not obtained because of the unavailability of the samples during the experiments. If the SRIM simulation results represent the as-implanted condition, the NDP results imply that $1000\,^\circ C$ annealing drives He diffusion to depths >$150\,nm$ while maintaining the He peak positions near the sample's surface. However, the calculated spatial accuracies of the measured He profiles must be assessed. Notably, the leading edge of NDP data, which is the surface of W in this case, is subject to spectral broadening. This can cause the data points to appear on the negative side of the 0-depth position. The width of the leading edge is related to the resolution of the silicon barrier detector and the roughness of the sample surface, among other factors. This broadening differs from the signal broadening due to charged-particle straggling, which is discussed in this paper.

The acquired NDP spectrum represents a convolution of the actual energy distribution of the charged particles and the measurement system. Each component of the system, i.e., the detector, digital multichannel analyzer (MCA), and sample, introduces uncertainties that can broaden the energy profile relative to the measured energy of the charged particle. Two main energy-broadening contributions can be identified: (1) the overall detector energy broadening (referred to as σ_{det}) represented by a system resolution of $\approx 18\,keV$, and (2) energy straggling as the charged particles travel through the sample material (σ_{strag}). GEANT4 Monte Carlo simulations [32] were conducted to evaluate critical parameters, such as sample geometry, detector solid angle, proton particle incident angle, nuclear-stopping power, and electronic-stopping power, to assess the energy straggling of energetic p traveling through the W sample. Table 2 lists the σ_{strag} resulting from the $572\,keV$ p emission from a W depth of $50\,nm$ to $500\,nm$. As the depth of the emitted proton increases, the resulting energy broadening increases from $2.7\,keV$ ($50\,nm$ depth) to $8.7\,keV$ ($500\,nm$ depth). Notably, the energy broadening caused by the sample material is much smaller than that caused by the detector system because the system resolution ($\approx 18\,keV$) is much larger than the straggling-induced broadening.

The effect of energy broadening on the actual data collected from the NDP detector system can be approximated using the detector response function R(x), assuming that a

Depth of emitted proton in W (nm)	σ_{strag} (keV)
50	2.7
100	3.8
200	5.3
500	8.7

Table 2. Estimated straggling-energy broadening of the 572 keV p transmitting through W with various depths, as calculated by GEANT4 model.

Gaussian model can describe the energy-broadening effects [33]:

$$R_i x = \frac{k}{2}[erf(\frac{E_i + \Delta - \bar{E}(x)}{\sqrt{2}\,\sigma_{E(x)}}) - erf(\frac{E_i - \Delta - \bar{E}(x)}{\sqrt{2}\,\sigma_{E(x)}})]$$
(2)

where $\sigma_{E(x)}$ is the total standard deviation of the total energy-broadening effect ($\sigma_{\text{det}}+\sigma_{\text{strag}}$), Δ is one half the width of an MCA channel,$\bar{E}(x)$ is the average energy corresponding to a particle emitted from depth x, E_i is the mean energy of channel I, and k is a constant accounting for the neutron flux, neutron cross-section, and detection efficiency. Based on the detector response function and peak broadening effect computed using Eq(2), Figure 5 shows the normalized detector response curve of the 572 keV proton simulated as if produced inside W and transmitted through a 50 nm or 100 nm depth of W. Apparently, peak broadening does not change the peak position. For the 50 nm and 100 nm cases, the peak position was centered at 50 nm and 100 nm, respectively, after considering the peak-broadening effect. This is in good agreement with the experimental NDP values. Cooling the detector to cryogenic temperatures may be a viable method to reduce this broadening.

An ideal material (perfectly smooth and homogeneous) contributes significantly less to peak broadening in NDP data than the detector system. Considering the broadening of the sample material (i.e., perfect detection system), the width of the detector response peak (i.e., full-width half-maximum of the peak) extends only up to 50 nm for p coming from less than 100 nm within W. However, considering the detector resolution, the width of the detector response curve extends up to 200 nm, which is $\approx$ four times the broadening caused. Additionally, the analyzed samples are neither smooth (0.5 µm roughness) nor homogenous; both factors contribute to signal broadening. Because of these complications, deconvoluting the detector response from the measured raw NDP data is extremely difficult. Therefore, the NDP results presented in Figure 4 are expected to overestimate the ^{3}He depth in W, although the ^{3}He peak positions determined in NDP measurements are considered accurate.

Calculation of the depth scale of the NDP profile is another contributing factor to the observed broadening. NDP depth profile calculations were performed by inputting the estimated values of material atomic composition and densities into TRIM, running the simulation program, and then using the output results to calculate an energy-to-depth calibration equation. In this study, W has been assumed to be pure and polycrystalline with a theoretical density of 19.25 g · cm^{-3}.

These idealized parameters may not reflect the real conditions of the measured sample (e.g., the presence of bubbles or voids owing to implantation). Therefore, the reported NDP depth scale may be inaccurate. The total He calculation is not dependent on these parameters and should provide a good estimate of the total He within the W material before and after annealing. An important question related to the extent to which the ^{3}He spatial distribution changed following 1000 °C1000°C annealing is addressed below.
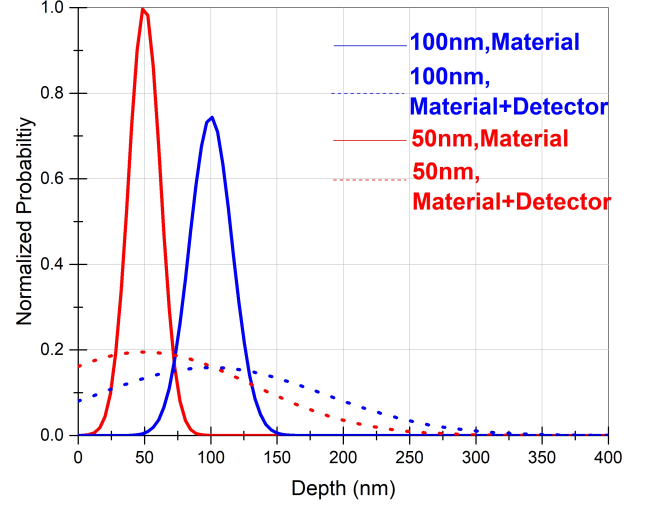

Fig. 5. (Color online) Normalized detector response of 572 keV proton ions from the ^{3}He(n,p)^{3}H reaction after traveling through 50 nm (red) or 100 nm (blue) of W, respectively, including broadening effects due to sample material only (SRIM results only, solid line), and due to material as well as detector system (dashed line).

C. LAMS experimental results

LAMS measurements were performed on the 10 keV, 10^{16} He cm^{-2} ^{4}He before and after 1 h, 1000 degreeCelsius annealing. The purpose was to assess the change in the spatial distribution of He following annealing at SI1000 degreeCelsius and to provide additional He depth profile data. Figure 6 shows the He concentration measured by LAMS compared with the SRIM simulation of the implanted He depth dependence for the 10 keV and 10^{16} He cm^{-2} implantation conditions. The uncertainty bars shown in Figure 6 are calculated by averaging the measurements from multiple laser ablation positions. They are dominated by the fluctuation of the He concentration measured at different positions and are reported to be 1σ, significantly larger than those calculated for the NDP measurements (based on one-spot measurement and calculated from experimental counting statistics). In the as-implanted condition, the He concentration measured by LAMS at depths of $\approx$ 20 nm and $\approx$ 30 nm agree with the simulated He implantation profile predicted by SRIM. Beyond 100 nm, the He concentration decreases to essentially zero (background level) in both the SRIM simulation and LAMS

measurement results.

He was not detected beyond $100\,\mathrm{nm}$ as well in the sample annealed at $1000\,^{\circ}\mathrm{C}$ for $1\,\mathrm{h}$. However, the measured He concentration in this sample decreased at near-surface depths in comparison with the as-implanted samples. This decrease was consistent with He diffusion to the surface, desorption, and some diffusion to greater depths. However, the LAMS measurements indicated that the diffusional broadening depth was less than $100\,\mathrm{nm}$, beyond which they did not indicate any significant He concentration. The center of the LAMS profile from the annealed sample was within a reasonable range, $25\,\mathrm{nm}$ and $45\,\mathrm{nm}$, the concentration peak estimated from the NDP data for the same sample.
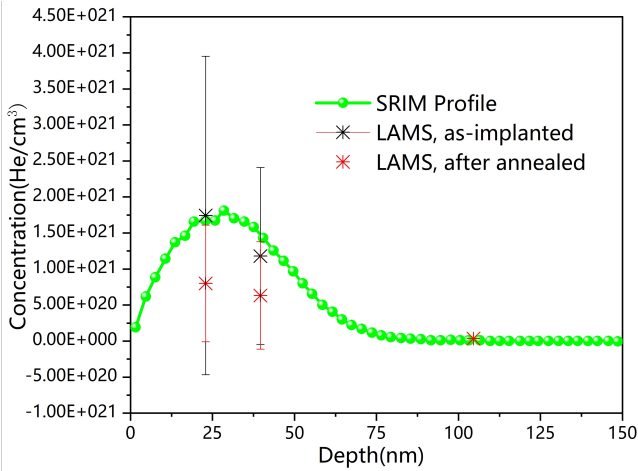

Fig. 6. (Color online) He concentration measured by LAMS for the implanted (black stars) and annealed (at $1000\,^{\circ}\mathrm{C}$ (red stars)) W samples, in comparison with SRIM (green circles) prediction of the implanted-He depth profile; the uncertainty is estimated from the crater volume created by the laser ablation (see text for details).

IV. CLUSTER DYNAMICS MODELING AND MODEL VALIDATION

A. He desorption process: Comparison between cluster dynamics modeling and experiment

The thermal $^{4}\mathrm{He}$ desorption spectrum from W implanted into 1×10^{16} He cm^{-2} during the heat treatment process was first reproduced using the model to evaluate the applicability of the default energetics and kinetic parameters. The blue line in Figure. 7 represents the simulated desorption spectra. The binding energies of the He_nV_m clusters shown in Figure 7(a) have been predicted using the initial default values based on ab initio simulations and extrapolation to larger clusters. The simulated curve in Figure 7(b) results from the optimization of the He_nV_m binding energies, and the resulting values are listed in Table 3.

Figure 7(a) illustrates the cluster dynamics model using the initial parameterization. The model predicts several peaks in the TDS data. However, the quantitative peak heights of the predicted He release flux were approximately one order of magnitude higher than those measured experimentally. The He binding energies of the small He_nV_m clusters were optimized based on the hypothesis that the presence of impurities within the W samples could affect the binding and diffusional kinetic energetics. The revised parameters are presented in Table 3. With the same set of optimized values, the model was in good agreement for all three implantation fluences in terms of the peak number, position, and intensity.

Figure 8 shows the simulated TDS spectra compared to the experimental results for the W samples implanted with $^{4}\mathrm{He}$ at three different fluence levels using the same optimized parameter set. The intensities of the $1000\,^{\circ}\mathrm{C}$ desorption peaks are in good agreement with the experimental results at each fluence. The $200\,^{\circ}\mathrm{C}$ He desorption peaks, incompletely developed peaks in the linear temperature ramping process, and decreasing He flux in the $1000\,^{\circ}\mathrm{C}$ annealing stage were also successfully captured using this model. A small desorption shoulder from $580\,^{\circ}\mathrm{C}$ to $700\,^{\circ}\mathrm{C}$ was predicted by the cluster dynamics model; however, this peak was only observed in the TDS measurement of the highest fluence sample.

Clusters	Ab initio and extrapolation(eV) (Figure. 7(a))	Optimized value(eV) (Figure. 7(b))
HeV	4.61	5.00
He_6V	2.56	3.10
He_8V	2.41	3.00
He_8V	2.25	2.90
He_9V_2	3.15	3.80
$He_{10}V_2$	2.89	3.50
$He_{11}V_2$	3.17	3.70
$He_{12}V_2$	2.67	3.30
$He_{13}V_2$	2.73	3.40
$He_{14}V_2$	2.61	3.20
$He_{15}V_2$	2.58	3.30

Table 3. Comparison of the binding energies (eV) of He to small He–V clusters

The measured He desorption spectrum results from the thermally driven evolution of all the clusters present in the W samples. The cluster dynamics model predicts that the cluster distribution would qualify before and after the major He desorption peaks at $25\,^{\circ}\mathrm{C}$, $250\,^{\circ}\mathrm{C}$, and $1000\,^{\circ}\mathrm{C}$. This analysis was performed to identify the primary clusters contributing to each He desorption peak. The He–vacancy cluster distributions at these three peak positions at a depth of $30\,\mathrm{nm}$ below the W surface are shown in Figure 9. The model predicts a majority of He interstitial clusters containing 6 He atoms to 8 He atoms as well as He-V complexes with 1 He atom to 9 He atoms (Figure 9(a)) with heating to $25\,^{\circ}\mathrm{C}$ following the implantation. At $250\,^{\circ}\mathrm{C}$, following the first desorption peak, the concentrations of He_6, He_7V, He_8V, and He_8V are the most significant. Following the major He desorption in the linear temperature ramping process and high-temperature annealing, He_xV_2 ($3 \leq x \leq 15$) clusters develop owing to the evolution of the mobile species. The model indicates that the dissociation of He_8 is the largest contributor to the He
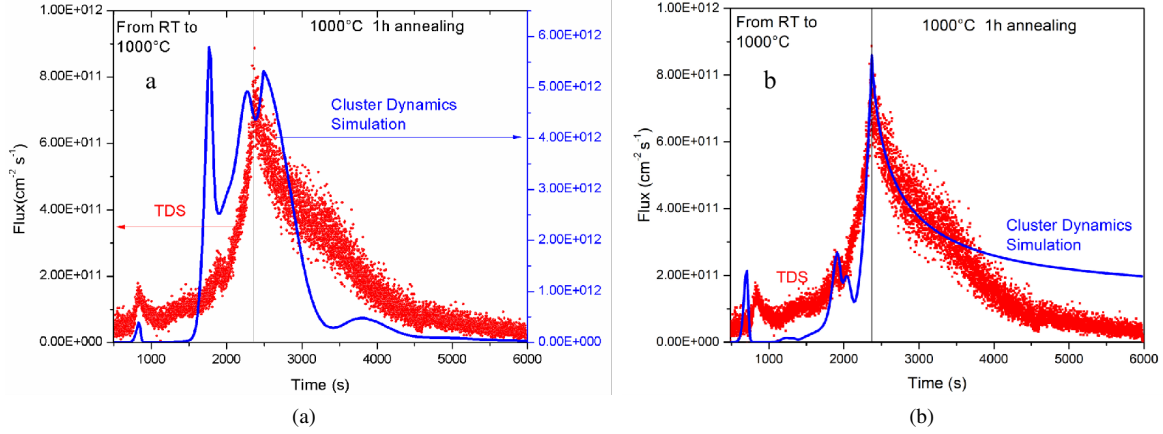
(a)

(b)

Fig. 7. (Color online) He desorption spectrum of 1×10^{16} ^{4}He cm^{-2} implanted W during $1000\,^\circ$C 1 h annealing process measured by TDS (red dots) and simulated by cluster dynamics model (blue curves). Simulation curve based on (a) He$_n$V$_m$ binding energies from ab initio and extrapolation, and (b) an optimized parameter set. Uncertainty is based on the equipment calibration and is less than 5%.
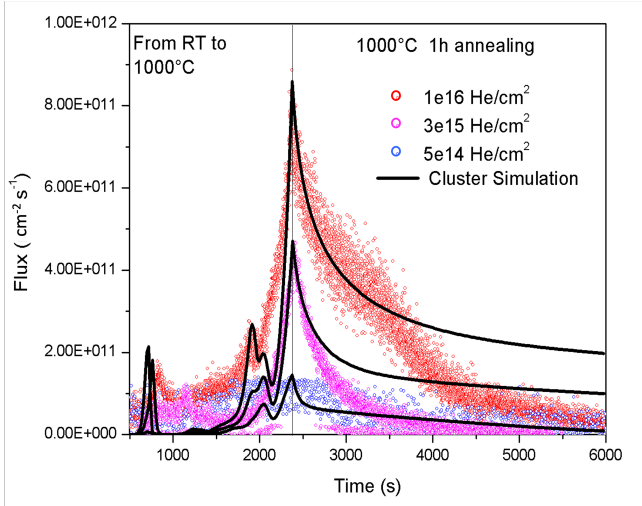

Fig. 8. (Color online) ^{4}He desorption spectra from W implanted at fluences of 5×10^{14} He cm^{-2}, 3×10^{15} He cm^{-2}, and 1×10^{16} He cm^{-2} during $1000\,^\circ$C 1 h annealing process measured by TDS (circles) and simulated by cluster dynamics model (solid line). Uncertainty is based on the equipment calibration and is less than 5%.

desorption peak at $200\,^\circ$C when comparing the change in the He-V cluster concentration from $25\,^\circ$C to $250\,^\circ$C (Figure 9(a) and 9(b), respectively). Between $250\,^\circ$C and $1000\,^\circ$C (Figure 9(b) and 9(c), respectively) the model indicates that the dissociation of He$_7$V, He$_8$V and He$_8$V are responsible for the main He release peak. Notably, at this implanted He fluence, the evolution of He-vacancy clusters in W was not significant, indicating that these clusters were relatively stable. This was expected based on the large binding energies of He to the He–V complexes listed in Table 3. The thermal stability of He–V clusters strongly depends on the He/V ratio in W [10, 34]. This phenomenon has also been observed in other material systems such as Fe [35, 36] and Ni [37]. Based

on the above analysis, the cluster dynamics model suggests that the major desorption peak at high temperatures is mainly caused by He desorption from the dissociation of He–V complexes, whereas the low-temperature desorption features are due to desorption from weak He sinks, such as dislocations. Transmission electron microscopy studies in other TDS experimental studies under similar implantation conditions [38] also confirm the above deduction.

B. He Depth profiling: Comparison between cluster dynamics modeling and experiments

The ^{3}He concentration profile in W was simulated using a cluster dynamics model. The atomic mass difference between the two He isotopes influenced only the diffusivity ($2D_{He_4} = \sqrt{3}D_{He_3}$), whereas the binding energies in the model did not change. The other difference was the spatially dependent Frenkel pair production and ^{3}He depth profiling calculated using SRIM (See Section II A Figure 1). Figure 10 compares the cluster dynamics modeling predictions with the NDP measurements. The NDP results indicate that the concentration of He for the 1×10^{16} He cm^{-2} peaked at a depth of 42 nm ($\pm$ 12 nm, 2σ, three-parameter Gaussian fit), which was statistically similar to the depth of the maximum He concentration predicted by the Monte Carlo simulations and within 3σ of the value estimated from the cluster dynamics model and LAMS experiment. However, as indicated above, an obvious discrepancy existed between modeling and NDP measurements concerning the ^{3}He spatial distribution for depths greater than 50 nm. The tail of the measured NDP spectra extended >200 nm, which could be attributed to energy broadening, detector resolution, and the use of idealized input parameters in the depth-scale calculations (see Section III B). Alternatively, cluster dynamics modeling predicted that He did not diffuse significantly beyond 75 nm.

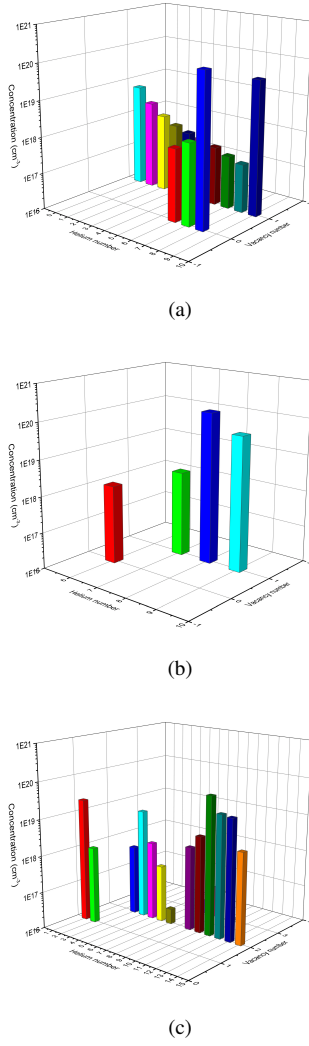The cluster dynamics model only accounts for the physical interaction between He and defect complexes as a func-

(a)

(b)

(c)

Fig. 9. (Color online) He_nV_m distribution predicted during thermal annealing by the cluster dynamics model following $10\,\mathrm{keV}$ ^{4}He implantation to 10^{16} atoms cm^{-2} using optimized cluster binding energies at a depth of $30\,\mathrm{nm}$ below the W surface, for the peak desorption temperatures of (a) $25\,^\circ$C, (b) $250\,^\circ$C, and (c) $1000\,^\circ$C. Uncertainty values were not calculated for these models.

Fig. 10. (Color online) ^{3}He depth profiles for W implanted by $10\,\mathrm{keV}$ ^{3}He after annealing at $1000\,^\circ$C for $1\,\mathrm{h}$ as a function of implantation fluence, measured by NDP (circles with dashed line to guide the eye, see Figure 4 for uncertainties) and simulated by cluster dynamics simulation without peak broadening effect (green, solid lines). Notably, the total He calculated from the NDP datasets is consistent with the estimated amount of He in each measured sample.

tion of the temperature (and ion implantation) conditions but does not explicitly model the experimental measurements using a synthetic diagnostic. While the NDP (curve dashed line in Figure 10) incorporates a convolution of cluster dynamics and peak broadening effects (based on the description in Section III B), the NDP experimental results show a similar peak width with dashed lines in Figure 5. The latter suggests that detector resolution, rather than He diffusion or interaction with the sample material, is the major cause for the measured He content beyond $100\,\mathrm{nm}$ observed in the NDP experiment. The total He calculated from the NDP datasets was statistically similar to that estimated for the measured samples. Therefore, NDP is a useful tool for quantifying the total implanted He in W metal.
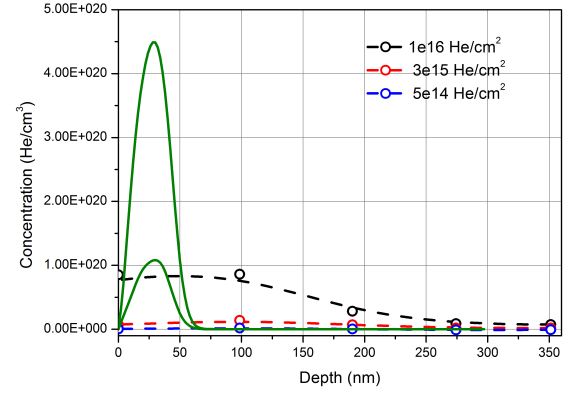
The comparison between the LAMS and cluster dynamics results further validates our conclusion that NDP data beyond $100\,\mathrm{nm}$ result predominately from detector resolution-induced broadening. Figure 11 shows the ^{3}He distribution in W implanted with $10\,\mathrm{keV}$ He ions at a fluence of 1×10^{16} He cm^{-2} before and after annealing at $1000\,^\circ$C for $1\,\mathrm{h}$, simulated by cluster dynamics model. The SRIM results for as-implanted samples and the LAMS results for as-implanted and annealed 1×10^{16} He cm^{-2} are also shown in Figure 11 for comparison. Apparently, for the 1×10^{16} He atom cm^{-2} sample after annealing, LAMS detects no discernable He in the implanted W samples beyond a depth of SI100nm, which is consistent with the cluster dynamics simulation results. Furthermore, the magnitude of the He concentration measured using the LAMS is reasonably consistent with the model prediction.

The cluster dynamics predicts that the spatial distribution of He in the as-implanted samples has a similar distribution as the He depth distribution predicted by SRIM, which has been used as the input for the model. This is rationalized by the fact that the implantation is conducted at room temperature, at which the mobility of the species is limited. However, an obvious discrepancy between these two models for the as-implanted condition is that the deeper tail of the He distribution simulated by the cluster dynamics model shifts toward the surface, and the peak width is narrower compared with the SRIM result. This is because of the strong trapping capacity of the vacancy defects in the damaged area, which act as sinks for mobile interstitial He atoms. In the cluster dynamics simulations, the depth-dependent production rates of the He and Frenkel pairs are obtained from SRIM and used as inputs.

The cluster dynamics simulation predicted that the He concentration decreases over the entire implantation range after annealing at $1000\,^\circ$C for $1\,\mathrm{h}$. The He concentration at the
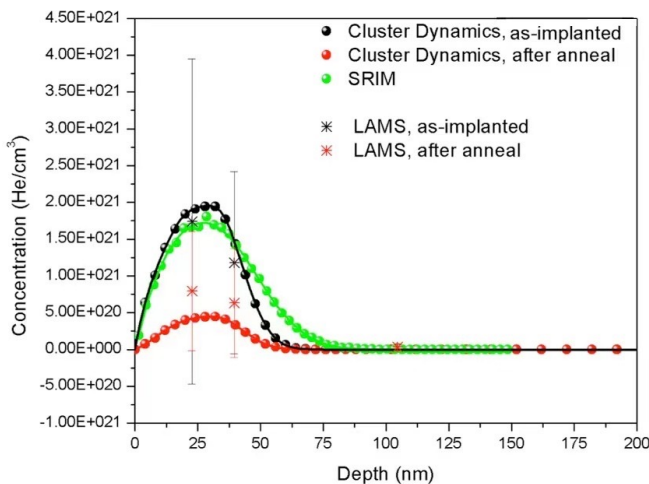
Fig. 11. (Color online) Cluster dynamics simulated (black and red filled circles) and SRIM (green circles)He depth-dependent profile of W implanted at a fluence of 1×10^{16} He cm^{-2}. The experimentally measured LAMS results are also shown as black and red symbols, respectively, for comparison.

peak position decreased by approximately four times during thermal annealing, although the depth of the maximum He concentration remained unchanged at $\approx 25\,\text{nm}$. This change agrees with the calculated amount of ^{3}He measured for the NDP samples. The simulation results agree reasonably well with the LAMS experimental observations, both in terms of the spatial depth dependence of He and the absolute magnitude of the He concentration. Furthermore, both cluster dynamics and LAMS measurements indicate that a limited amount of He diffuses past $75\,\text{nm}$ below the W surface. Therefore, the decrease in the He concentration within the implanted region is mainly caused by He desorption from the surface and not by He diffusion from the damaged regime deeper into bulk W.

Examination of the He-defect cluster distribution before and after annealing from the cluster dynamics simulation reveals that the dominant cluster configurations of the desorbed He are He interstitials and some relatively weaker bound He-vacancy defect clusters. During annealing, the motion of these highly mobile species is predominantly controlled by the concentration gradient of He. Because the concentration gradient is considerably steeper in the near-surface region than in the deeper bulk region, He diffuses more readily to the surface and desorbs from the sample.

C. Isotopic effect: Comparison of ^{3}He and ^{4}He desorption behavior by cluster dynamics modeling

Because of the strong background signal of the mass/charge of three in the TDS system, the thermal ^{3}He desorption spectra were not measured, and TDS measurements were used instead of ^{4}He with equivalent implantation and thermal annealing conditions. Here, we describe the cluster dynamics modeling results to investigate any differences in the desorption behavior. The simulated TDS curves for ^{4}He and ^{3}He implanted with W under the same implantation and heat treatment conditions are shown in Figure 12. As evident, the difference between the two predicted desorption spectra is subtle. The relatively smaller He desorption magnitude of ^{3}He results from the smaller damage production rate and larger backscattered fraction based on SRIM calculations. The higher mobility of ^{3}He also leads to a slight shift in the He desorption peaks to a lower-temperature regime. Overall, the differences between the predicted thermal desorption of ^{3}He and ^{4}He are insignificant; therefore, using ^{3}He to study the depth profiling of He in W is reasonable.
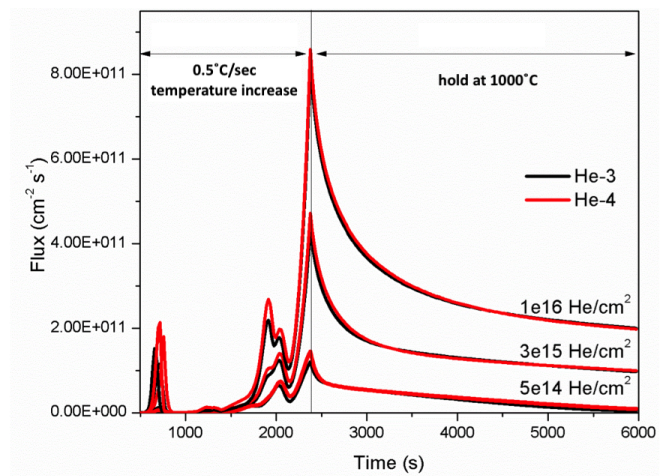

Fig. 12. (Color online) Cluster dynamics simulated TDS spectra for ^{3}He (black)- and ^{4}He (red)-implanted W, as a function of time and implanted He fluence. Uncertainty values were not calculated for these models.

V. CONCLUSIONS

We described the results of our investigation of the behavior of He in W following $10\,\text{keV}$ He implantation and thermal annealing through coordinated experimental characterization and cluster dynamics simulations. He retention and depth dependence were evaluated by TDS, NDP, and LAMS. TDS was used to measure the desorbed He during thermal annealing of the samples, whereas NDP and LAMS measured the He depth profile. These three experimental measurements provided a platform to validate the energetic and kinetic parameters of He interstitial and He-V clusters from atomistic simulations using a cluster dynamics model. The cluster dynamics model could reproduce the experimental results well, following the optimization of the binding energies of relatively small He-V clusters. The most significant difference between the model predictions and NDP experimental results was related to the depth distribution of He beyond $75\,\text{nm}$ below the W surface because of the NDP detector energy resolution and sample morphology. However, NDP results were useful for calculat-

ing the total He concentration for each sample set and were in good agreement with the LAMS and model results. The TDS measurements during annealing at $1000\,^\circ$C for $1\,$h were consistent with an incompletely developed desorption peak at $1000\,^\circ$C. The cluster dynamics model using the optimized He-V binding energies agreed well with the measured TDS data. Finally, the resulting He-V cluster energetics and cluster dynamics model provided insight into the dissociating clusters responsible for the measured desorption peaks and would be useful for future modeling of He cluster evolution in W because of $14\,$MeV neutron irradiation in the burning fusion environment.

VI. ACKNOWLEDGEMENTS

VII. REFERENCE

[1] G. Janeschitz, I. Jct et al., Plasma–wall interaction issues in iter. J. Nucl. Mater. **290**, 1–11 (2001). doi:10.1016/S0022-3115(00)00623-1

[2] L.R. Greenwood, R.K. Smither, Specter: neutron damage calculations for materials irradiations. . doi:10.2172/6022143

[3] Z. Xu, Z.W. Wu, L. Zhang et al., Tungsten control in type-i elmy h-mode plasmas on east. Nucl. Sci. Tech. **32**, 95 (2021). doi:10.1007/s41365-021-00929-4

[4] H.M. Şahin, G. Tunç, A. Karakoç et al., Neutronic study on the effect of first wall material thickness on tritium production and material damage in a fusion reactor. Nucl. Sci. Tech. **33**, 43 (2022). doi:10.1007/s41365-022-01029-7

[5] S. Zhang, Y.B. Nie, J. Ren et al., Benchmarking of jeff-3.2, fendl-3.0 and tendl-2014 evaluated data for tungsten with 14.8 mev neutrons. Nucl. Sci. Tech. **28**, 27 (2017). doi:10.1007/s41365-017-0192-0

[6] C. Li, B. Wang, Z.L. Zhang et al., Erosion of tungsten surfaces in he and ar/he plasma. Nucl. Sci. Tech. **27**, 1–5 (2016). doi:10.1007/s41365-016-0049-y

[7] R. Behrisch, V. Khripunov, R. Santoro et al., Transmutation of plasma facing materials by the neutron flux in a dt fusion reactor. J. Nucl. Mater. **258**, 686–693 (1998). doi:10.1016/S0022-3115(98)00249-9

[8] F. Sefta, K.D. Hammond, N. Juslin et al., Tungsten surface evolution by helium bubble nucleation, growth and rupture. Nucl. Fusion **53**, 073015 (2013). doi:10.1088/0029-5515/53/7/073015

[9] J. Boisse, A. De Backer, C. Domain et al., Modeling of the self trapping of helium and the trap mutation in tungsten using dft and empirical potentials based on dft. J. Mater. Res. **29**, 2374–2386 (2014). doi:10.1557/jmr.2014.258

[10] C. Becquart, C. Domain, An object kinetic monte carlo simulation of the dynamics of helium and point defects in tungsten. J. Nucl. Mater. **385**, 223–227 (2009). doi:10.1016/j.jnucmat.2008.11.027

[11] T. Faney, B. Wirth, Spatially dependent cluster dynamics modeling of microstructure evolution in low energy helium irradiated tungsten. Model. Simul. Mater. Sc. **22**, 065010 (2014). doi:10.1088/0965-0393/22/6/065010

[12] S. Blondel, D.E. Bernholdt, K.D. Hammond et al., Continuum-scale modeling of helium bubble bursting under plasma-exposed tungsten surfaces. Nucl. Fusion **58**, 126034 (2018). doi:10.1088/1741-4326/aae8ef

[13] L. Hu, K.D. Hammond, B.D. Wirth et al., Interactions of mobile helium clusters with surfaces and grain boundaries of plasma-exposed tungsten. J. Appl. Phys. **115**, 173512 (2014). doi:10.1063/1.4874675

[14] K.D. Hammond, S. Blondel, L. Hu et al., Large-scale atomistic simulations of low-energy helium implantation into tungsten single crystals. Acta Mater. **144**, 561–578 (2018). doi:10.1016/j.actamat.2017.09.061

[15] K. Sato, R. Tamiya, Q. Xu et al., Detection of deuterium trapping sites in tungsten by thermal desorption spectroscopy and positron annihilation spectroscopy. Nuclear Materials and Energy **9**, 554–559 (2016). doi:10.1016/j.nme.2016.09.014

[16] T. Faney, S.I. Krasheninnikov, B.D. Wirth, Spatially dependent cluster dynamics model of he plasma surface interaction in tungsten for fusion relevant conditions. Nucl. Fusion **55**, 013014 (2014). doi:10.1088/0029-5515/55/1/013014

[17] G. Shaw, W. Garcia, X. Hu et al., Investigating helium–deuterium synergies in plasma-exposed tungsten using laser ablation techniques. Phys. Scripta **2020**, 014029 (2020). doi:10.1088/1402-4896/ab47c7

[18] X. Hu, K.G. Field, S. Taller et al., Impact of neutron irradiation on thermal helium desorption from iron. J. Nucl. Mater. **489**, 109–117 (2017). doi:10.1016/j.jnucmat.2017.03.034

[19] R. Downing, G. Lamaze, J. Langland et al., Neutron depth profiling: overview and description of nist facilities. Journal of research of the National Institute of Standards and Technology **98**, 109 (1993). doi:10.6028/jres.098.008

[20] S.B. Gilliam, S.M. Gidcumb, D. Forsythe et al., Helium retention and surface blistering characteristics of tungsten with regard to first wall conditions in an inertial fusion energy reactor. Nucl. Instrum. Methods Phys. B **241**, 491–495 (2005). doi:10.1016/j.nimb.2005.07.060

[21] Z. Tun, J. Noël, T. Bohdanowicz et al., Cold-neutron depth profiling as a research tool for the study of surface oxides on metals. Can. J. Phys. **88**, 751–758 (2010). doi:10.1139/P10-062

[22] J.F. Ziegler, M.D. Ziegler, J.P. Biersack, Srim–the stopping and range of ions in matter (2010). Nucl. Instrum. Methods Phys. B **268**, 1818–1823 (2010). doi:10.1016/j.nimb.2010.02.091

[23] J. Ziegler, G. Cole, J. Baglin, Technique for determining concentration profiles of boron impurities in substrates. J. Appl. Phys. **43**, 3809–3815 (1972). doi:10.1063/1.1661816

[24] G. Shaw, M. Bannister, T.M. Biewer et al., The detection of he in tungsten following ion implantation by laser-induced breakdown spectroscopy. Appl. Surf. Sci. **427**, 695–703 (2018). doi:10.1016/j.apsusc.2017.08.180

[25] D. Xu, B.D. Wirth, Spatially dependent rate theory modeling of thermal desorption spectrometry of helium-implanted iron. Fusion science and technology **56**, 1064–1068 (2009). doi:10.13182/FST09-A9052

[26] D. Xu, B.D. Wirth, Modeling spatially dependent kinetics of helium desorption in bcc iron following he ion implantation. J. Nucl. Mater. **403**, 184–190 (2010). doi:10.1016/j.jnucmat.2010.06.025

[27] D. Xu, X. Hu, B.D. Wirth, A phase-cut method for multi-species kinetics: Sample application to nanoscale defect cluster evolution in alpha iron following helium ion implantation. Appl. Phys. Lett. **102**, 011904 (2013). doi:10.1063/1.4773876

[28] D. Xu, B.D. Wirth, M. Li et al., Combining in situ transmission electron microscopy irradiation experiments with cluster dynamics modeling to study nanoscale defect agglomeration in structural metals. Acta Mater. **60**, 4286–4302 (2012). doi:10.1016/j.actamat.2012.03.055

[29] X. Hu, D. Xu, T.S. Byun et al., Modeling of irradiation hardening of iron after low-dose and low-temperature neutron irradiation. Model. Simul. Mater. Sc. **22**, 065002 (2014). doi:10.1088/0965-0393/22/6/065002

[30] L. Hu, K.D. Hammond, B.D. Wirth et al., Molecular-dynamics analysis of mobile helium cluster reactions near surfaces of plasma-exposed tungsten. J. Appl. Phys. **118**, 0163301 (2015). doi:10.1063/1.4933393

[31] C.S. Becquart, C. Domain, U. Sarkar et al., Microstructural evolution of irradiated tungsten: Ab initio parameterisation of an okmc model. J. Nucl. Mater. **403**, 75–88 (2010). doi:10.1016/j.jnucmat.2010.06.003

[32] S. Agostinelli, J. Allison, K.a. Amako et al., Geant4—a simulation toolkit. Nuclear instruments and methods in physics research section A: Accelerators, Spectrometers, Detectors and Associated Equipment **506**, 250–303 (2003). doi:10.1016/S0168-9002(03)01368-8

[33] J.T. Maki, R.F. Fleming, D.H. Vincent, Deconvolution of neutron depth profiling spectra. Nucl. Instrum. Methods Phys. B **17**, 147–155 (1986). doi:10.1016/0168-583X(86)90077-7

[34] C. Becquart, C. Domain, Ab initio calculations about intrinsic point defects and he in w. Nucl. Instrum. Methods Phys. B **255**, 23–26 (2007). doi:10.1016/j.nimb.2006.11.006

[35] K. Morishita, R. Sugano, B.D. Wirth et al., Thermal stability of helium–vacancy clusters in iron. Nucl. Instrum. Methods Phys. B **202**, 76–81 (2003). doi:10.1016/S0168-583X(02)01832-3

[36] C.C. Fu, F. Willaime, Ab initio study of helium in α- fe: Dissolution, migration, and clustering with vacancies. Phys. Rev. B **72**, 064117 (2005). doi:10.1103/PhysRevB.72.064117

[37] D. Hepburn, D. Ferguson, S. Gardner et al., First-principles study of helium, carbon, and nitrogen in austenite, dilute austenitic iron alloys, and nickel. Phys. Rev. B **88**, 024115 (2013). doi:10.1103/PhysRevB.88.024115

[38] Q. Xu, J. Zhang, K. Maejima et al., Retention and thermal desorption of helium in pure tungsten. Phil. Mag. Lett. **96**, 477–481 (2016). doi:10.1080/09500839.2016.1260175